Structural changes and the metal-non-metal transition in supercritical fluids

TOPICAL REVIEW

Structural changes and the metal–non-metal transition in supercritical fluids

Kozaburo Tamura and Masanori Inui

Faculty of Integrated Arts and Sciences, Hiroshima University, Higashi-Hiroshima 739-8521, Japan

Abstract
Energy-dispersive x-ray diffraction (XD), small-angle x-ray scattering (SAXS) and x-ray absorption fine-structure (XAFS) measurements for metallic fluids up to the supercritical region were carried out using synchrotron radiation. We obtained the structure factor $S(k)$ and the pair distribution functions $g(r)$ for expanded fluid Hg from the liquid to the dense vapour region including the metal–non-metal (M–NM) transition region in the density range from 13.6 to 1.9 g cm^{-3} by means of XD measurements at SPring-8 in Japan. The density variations of the interatomic distance (r_1) and coordination number (N_1) obtained are discussed in relation to the M–NM transition in fluid Hg. To investigate structural change in the semiconductor–metal (SC–M) transition in expanded fluid Se, XD measurements, at SPring-8, and XAFS measurements, at the European Synchrotron Radiation Facility (ESRF) in France, were carried out at high temperatures and high pressures. It was found that the twofold-coordinated chain structure is preserved and contraction of the covalent bond occurs on the SC–M transition. XAFS measurements for dense Se vapour near the critical point were also carried out to study how dimers in the rarefied vapour condense to the metallic fluid. SAXS measurements were carried out to obtain information on the density fluctuation of fluid Se near the critical point. On the basis of the structural data obtained by XD, XAFS and SAXS measurements for fluid Se, we discuss how the density fluctuation affects the local structure and electronic properties of fluid Se near the critical point.

1. Introduction

A substantial and continuous volume expansion from liquid to rarefied vapour occurs with the change of temperature and pressure surrounding the liquid–vapour critical point without crossing the saturated-vapour-pressure curve as shown in figure 1. Many investigations have been carried out so far with molecular fluids and several variations of the equation of state including the supercritical region have been advanced since the work by van der Waals. In the expansion process the mean interatomic distance increases to up to ten times larger than that under normal conditions. However, drastic changes such as reconstitution of the molecular
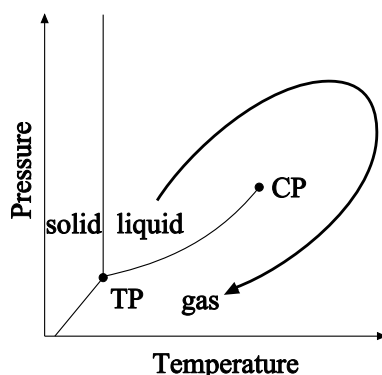
Figure 1. A schematic phase diagram on the pressure–temperature plane. TP and CP denote the triple point and the liquid–vapour critical point, respectively.

unit hardly occur in molecular fluids. On the other hand, in the expansion process of metallic or semiconducting liquids, physical properties are dramatically changed. Liquid Hg, well known as a prototype liquid metal, undergoes a metal–insulator transition when the density is reduced to about 9 g cm^{-3} near the critical point [1]. Liquid Se, which is the only elemental liquid that is a semiconductor and which has a twofold-coordinated chain structure where atoms are covalently bonded, also experiences a semiconductor–metal–insulator (SC–M–I) transition around the critical point.

It is obvious that information on the atomic arrangement of these metallic fluids is quite important for the understanding of the mechanism of the metal–non-metal (M–NM) transition. However, structural studies such as diffraction experiments on metallic fluids are not easy to carry out because the critical temperature and pressure are very high compared with those for molecular fluids. For many decades there have been almost no structural studies of supercritical metallic fluids except for fluid Rb and Cs. The static and dynamic structures of fluid Rb and Cs, whose critical pressures are low compared with that of, for example, fluid Hg, were investigated in the pioneering works of Hensel and co-workers using neutrons [2].

Recently Tamura and Hosokawa developed a high-pressure vessel with Be windows and a specially designed sapphire cell with which we are able to perform structural studies of metallic fluids at high temperatures and high pressures [3–9]. This technique is widely applicable to a variety of structural studies as seen in the following section. In fact, Tamura and Hosokawa succeeded in measuring x-ray diffraction, using an in-house x-ray source, for expanded fluid Hg in the metallic region and also up to the critical region. They obtained information about the density variation of the first-neighbour coordination.

To get more information on the higher-order structural correlation—such as the second- and third-neighbour coordination—of metallic fluids it is essential and powerful to perform x-ray experiments using a synchrotron radiation source instead of an in-house x-ray source. Synchrotron radiation is quite strong and directional in character. Combining our high-temperature and high-pressure techniques with synchrotron radiation, we have a greater possibility of getting data of high quality on the microscopic structures—including the dynamic structure as well as the static one—of supercritical metallic fluids.

In this paper we present results of x-ray diffraction (XD) measurements for fluid Hg and Se extending from the liquid to the dense vapour region beyond the liquid–vapour critical point, and small-angle x-ray scattering (SAXS) measurements for fluid Se near the critical point, using synchrotron radiation at the super-photon ring operating at 8 GeV (SPring-8) in Japan.

Results of x-ray absorption fine-structure (XAFS) spectroscopy for fluid Se, carried out at the European Synchrotron Radiation Facility (ESRF) in France, are also presented.

2. Experimental procedure

2.1. X-ray diffraction measurements

2.1.1. Experimental apparatus. We have performed energy-dispersive x-ray diffraction measurements using synchrotron radiation on the beamline BL-04B1 at SPring-8. The storage ring was operated at 8 GeV and 20 mA in 1997 and the current becomes 100 mA in present operation. White x-rays were generated through the bending magnet ranging in energy to 150 keV. In the experimental hutch we have a high-pressure generation system including a gas compressor, a high-pressure vessel and a chiller and an energy-dispersive x-ray diffractometer. The diffractometer is composed of a goniometer, adjustable stages and a pure-Ge solid-state detector (SSD). This technique has been employed in our in-house structural studies of expanded fluids [3–12].

In the energy-dispersive method, white x-rays were used as the primary beam, and the scattered photons were detected and energy analysed by the SSD. Figure 2 shows a schematic diagram of the diffractometer. A horizontal goniometer system was installed, in which an x-ray source and a detector were set in a horizontal plane. The signals of the scattered x-rays detected by the SSD were received with a multichannel pulse-height analyser (MCA). Energy-dispersive measurements were performed at a fixed scattering angle (2θ) and the angles were selected to cover a sufficiently wide range of scattering wavenumber k, where $k = (4\pi \sin\theta/hc)E$ (E: photon energy; h: Planck's constant; c: velocity of light).
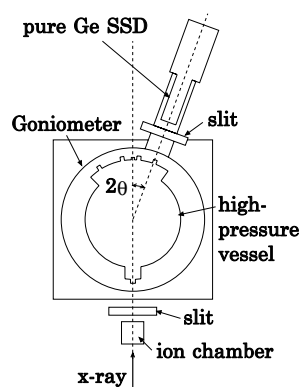

Figure 2. A schematic diagram of the diffractometer in the BL04B1 beamline at SPring-8 for energy-dispersive x-ray diffraction experiments.

The size of the x-ray beam was made smaller, down to 0.2×0.2 mm^2, using the horizontal and vertical tungsten slits in the optical hutch in the upper stream. The beam was directly introduced into the high-pressure vessel mounted on a goniometer through a Be window for the vessels, which are illustrated in figure 3.

The experimental conditions at high temperature and high pressure were achieved with an internally heated high-pressure vessel made of a super-high-tension steel. Figure 3(a) shows a side view of the high-pressure vessel for x-ray diffraction measurements using synchrotron radiation and it permits experimental conditions up to 1700 °C and up to 2000 bar including the supercritical region of fluid Hg [15]. The vessel is constructed of a main cylinder with inner
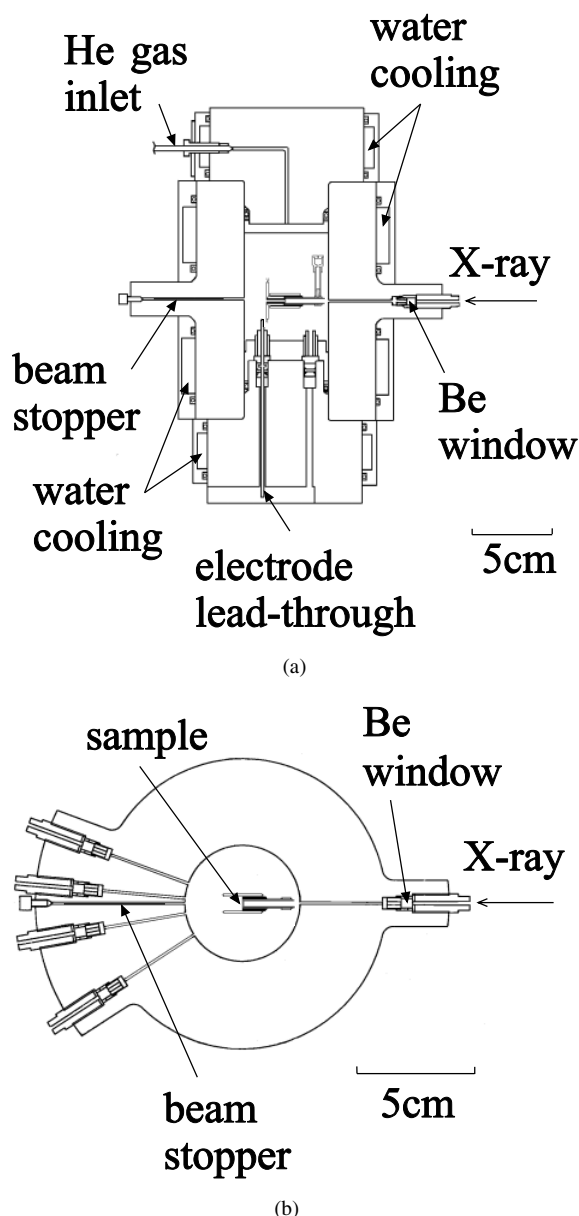
(a)

(b)

Figure 3. (a) A side view of the high-pressure vessel for energy-dispersive x-ray diffraction experiments. (b) A top view of the first high-pressure vessel with four windows for scattered x-rays. (c) A top view of the second high-pressure vessel with seven windows for scattered x-rays.

diameter of 50 mm, outer diameter of 105 mm and length of 140 mm, and two flanges with thicknesses of 43 and 49 mm. These flanges are supported by a press-frame when the vessel is pressurized by high-purity-grade (99.9999%) He gas which has a low absorption constant for x-rays in the energy range of the present experiment. A rubber O-ring is used for pressure sealing. The sample is located on the central axis of the high-pressure vessel and the sapphire cell is held by alumina discs which are not illustrated in the figure. The primary and scattered
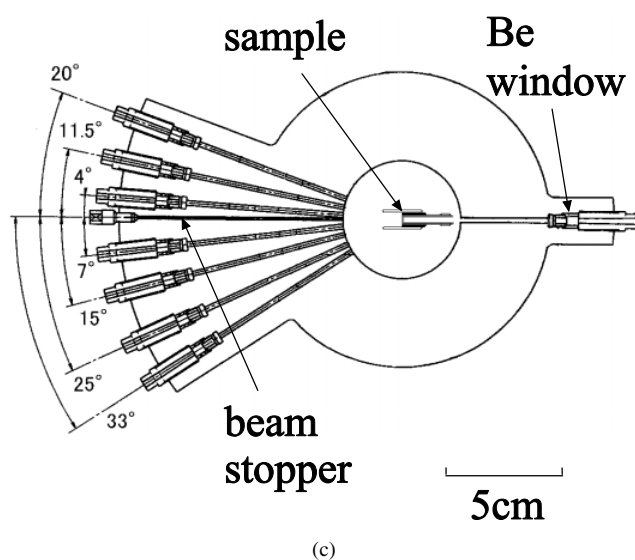
Figure 3. (Continued)

x-ray beams passed through Be windows with thickness of 5 mm and diameter of 4 mm. Each of the Be windows is supported by the flat area of a back-up screw. There were five Be windows, one of which is for the primary x-ray beam and the rest for the scattered ones, which are located at 2θ-values of 5°, 10°, 20° and 33° for the first vessel as shown in figure 3(b). We have made a new high-pressure vessel to improve the observed spectra and since 2000 we have used the second vessel which has seven windows for the scattered x-rays, located at 4°, 7°, 11.5°, 15°, 20°, 25° and 33° as shown in figure 3(c). The highest pressure permitted by the new vessel is also 2000 bar. The second vessel has a minimum scattering angle of 4°, where one can observe a structure factor at smaller k than in the experiments using the first one. The electrodes for the heaters and thermocouples are brought out of the vessel through the lower flange, where Bridgman-type high-pressure seals are used. Pressure is measured with a Heise gauge, having an accuracy of ± 3 bar. Water cooling jackets are placed around the outside of the vessel.

Supercritical metallic fluids such as Hg and Se must be contained in a cell made of a special material that is transparent to x-rays and resistant to chemical corrosion by hot metallic fluids. A single-crystal sapphire cell was developed for this purpose and the details are illustrated in figure 4(a). The cell consists of a hot part heated by a surrounding W heater and a sample reservoir kept at around the melting temperature of the liquid sample. The construction around the hot part is shown in figure 4(b) on an enlarged scale. A closed-end sapphire tube with an inner diameter of 2.5 mm, an outer diameter of 3.2 mm and a length 21.4 mm was put into another closed-end tube with an inner diameter of 3.2 mm, an outer diameter of 4.0 mm and a length of 20.5 mm. The sapphire components were connected with a high-temperature ceramic adhesive (SEM-COM Company Incorporated, type SCE-1) providing a uniform gap between the closed ends of the tubes. The thickness of the closed end of each tube was 150 μm and the gap was fixed to give a suitable sample thickness from 30 μm to 500 μm.

In measuring x-ray diffraction from the fluid sample contained in the sample cell, the problem was how to discriminate the strong diffraction from the sapphire cell. This was overcome by employing the following procedure on assembling the cell. First of all, both
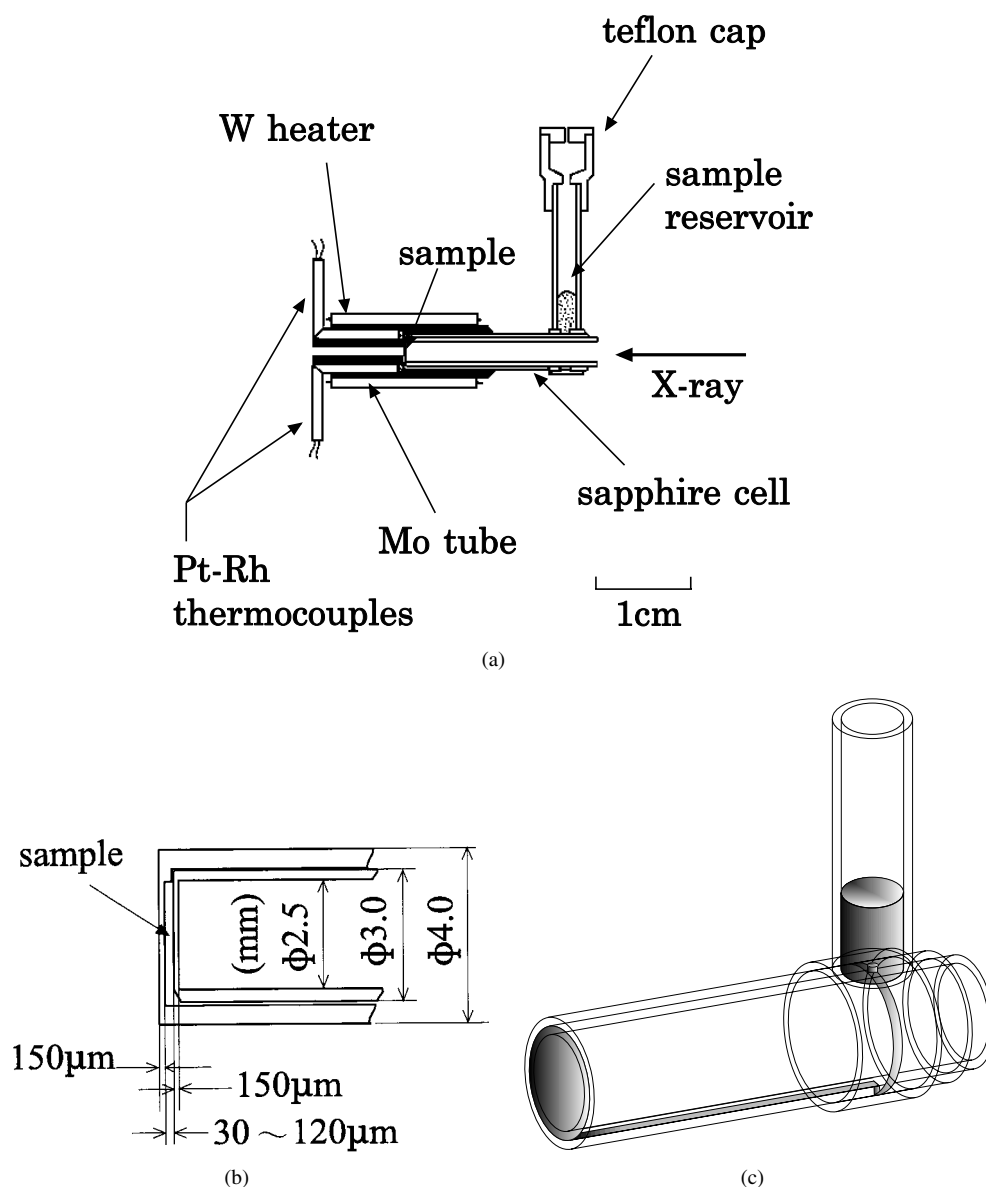
(a)

(b)

(c)

Figure 4. (a) The construction of the sapphire cell used for the present x-ray diffraction experiments. (b) Details of the sample space shown on an enlarged scale. (c) A schematic illustration of the path that the liquid sample takes from the reservoir.

the inner and outer closed-end tubes were made from the same rod cut off from a sapphire plate along the c-axis such that their c-axes were parallel to the direction of the primary x-ray beam and Laue spots with a nearly triple symmetry from the closed ends had the same pattern. After observing the Laue pattern of each closed end, the most appropriate direction around the c-axis could be chosen where no Laue spots were observed through the Be windows of the high-pressure vessel. When one applies this procedure, the detected x-rays should, at least in principle, have no Bragg or coherent components originating from the sapphire cell.

The cell was heated by a heating element made of W wire with a diameter of 0.4 mm. The W heater was set around a Mo tube. As a slit was made on the left-hand side of the Mo tube in figure 4(a), scattered x-rays were able to go out through it. The temperature of the sample was measured by two Pt–30% Rh:Pt–6% Rh thermocouples, which were inserted in the holes of the Mo tube and were in close contact with the wall of the closed end of the outer sapphire tube. In the case of selenium, the sample reservoir was covered by a copper cap surrounded by a heating element made of Mo wire 0.3 mm in diameter and the temperature was measured by Ni–Cr:Ni–Al thermocouples. The cell and the heaters were supported by alumina discs. Special care was taken to construct the alumina discs such that the sample was precisely positioned on the central axis of the vessel. The space between the alumina discs and the inner wall of the vessel was filled with alumina powder to obtain good thermal insulation and to prevent convection of the compressed He gas; the details of this are described in the literature [12].

The procedure for filling the sample space between the closed ends of the cell with metallic fluids is as follows. First, liquid Hg or solid selenium was put into the sample reservoir. After closing the high-pressure seals, the entire assembly was evacuated. In the case of selenium, the W heater is heated up to 300 °C and the Mo heater around the sample reservoir is heated up to 270 °C. The high-pressure vessel was then pressurized using He gas at 2 or 3 bar, which was sufficient to force liquid sample through a small channel between the outer and inner sapphire tubes to fill the sample space as shown in figure 4(c). Once the cell had been filled, the temperature of the reservoir was maintained above the melting temperature of the sample. Pressure balance between the compressed fluid sample and He gas was achieved through the liquid surface in the reservoir. The purity of the sample was 99.9999% for Hg and 99.999% for Se.

2.1.2. Data analysis. To obtain the structure factor, $S(k)$, of a metallic fluid from the experimental scattering intensity, several data corrections had to be made such as taking account of the escape effect of the detector, the energy spectrum of the primary beam, the absorption by the sapphire cell, compressed He gas, the Be windows and the metallic fluid itself, and finally Compton scattering from the sample and the sapphire cell.

First we performed the correction for the escape effect of the Ge SSD. The escape yield obtained experimentally was given in our instrumental paper [12]. The correction for the escape effect was performed using the method reported by Nishikawa and Iijima [16].

As is well known for x-ray diffraction measurements using the energy-dispersive method, it is essential to know the energy spectrum of the primary beam $I_0(E)$. In the present experiment, $I_0(E)$ was determined by measuring the scattering from the empty sapphire cell with the same geometry around the cell and the same operating conditions for the synchrotron radiation as were used in the measurements on the sample. The measurements were carried out with the high-pressure vessel evacuated in advance of the sample measurements. The detailed procedure for getting the $I_0(E)$ spectrum was given in our previous paper [12]. Using the observed energy spectra of the empty cell at 2θ-values of 20°, 25° and 33°, we obtained the $I_0(E)$ spectrum.

We then measured the energy spectrum of x-rays scattered from the fluids contained in the sapphire cell. Figure 5 shows, as an example, the scattering intensity spectra at different angles of liquid Se at 300 °C obtained using the second high-pressure vessel. According to the procedure given in our previous paper [12], $S(k)$ was deduced for the sample. The observed total scattering intensity is the sum of the spectral intensity of the coherent and incoherent scattering from the sample, and the incoherent scattering from the sapphire cell. It should be noticed that the term concerned with the coherent scattering from the sapphire cell does
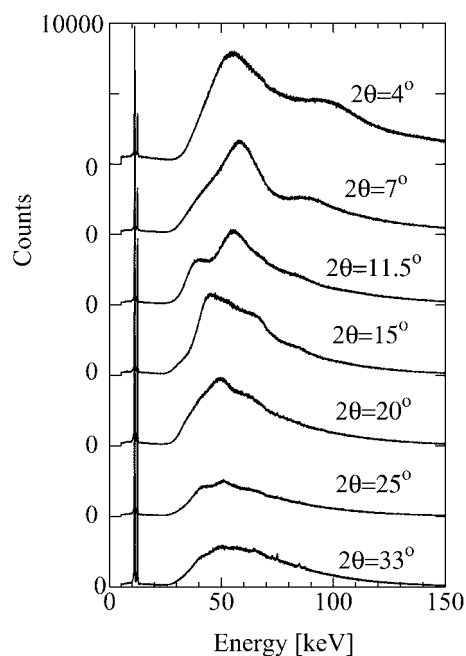
Figure 5. Observed scattering intensity at different angle settings for liquid Se at 300 °C and 10 bar.

not appear in the observed total-scattering spectrum in the way mentioned in the previous subsection. The multiple-scattering contribution was not taken into account. For estimating the incoherent scattering terms from the sample and the sapphire cell, the calculation was performed using several data such as the incoherent scattering intensity of the sample and sapphire [17, 18], densities, mass absorption coefficients [19] and thicknesses of the sample, the cell, the He gas and the Be windows, and the $I_0(E)$ spectrum. The coherent scattering term of the sample was obtained by subtracting these incoherent terms from the total-scattering spectrum. For calculating $S(k)$ from the coherent term of the sample, we used the atomic scattering factor of the sample given in the literature [20].

The $S(k)$ data at different angle settings were obtained as shown in figure 6. The overlap is excellent for all of the spectra and as a result of using spectra at seven scattering angles, a k-value in the middle range is based on at least three independent experimental results. $S(k)$ was finally obtained as the bottom spectrum in the figure.

Finally, we should comment that poorer crystallinity makes Laue spots broader and a weak diffraction peak which may come from the tail of the Laue peak is sometimes observed in the intensity spectrum. A small shoulder of the third peak in the $S(k)$ data at 20° in figure 6 is an example. When several curves overlap in the same k-region like in this case, the peak would be eliminated from the final $S(k)$. The new vessel is very useful for solving such problems and improving the reliability of the $S(k)$ data.

2.2. SAXS measurements

SAXS measurements were performed using synchrotron radiation on the beamline BL04B2 at SPring-8. This beamline is designed to facilitate diffraction and scattering experiments at high energy, more than 38 keV, on various kinds of material. White x-rays generated by a bending
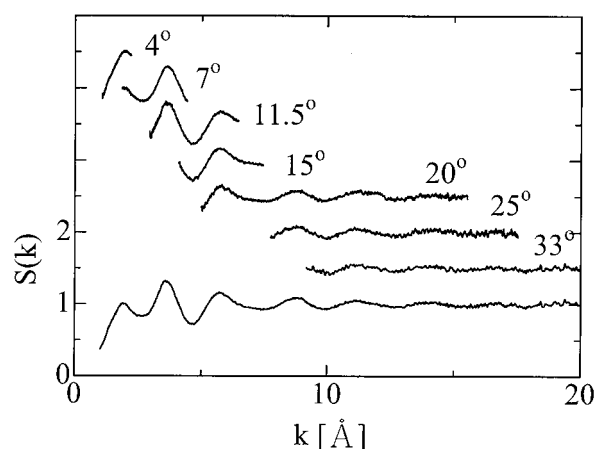
Figure 6. $S(k)$ data obtained at different angle settings for liquid Se at 300 °C and 10 bar. The bottom curve shows $S(k)$ obtained finally.

magnet are monochromatized by a bent crystal to focus a high-energy x-ray beam. The Bragg angle of the monochromator crystal is fixed at $2\theta = 6°$ in the horizontal plane. For small-angle x-ray scattering experiments, the flat surface of Si(111) was used. Monochromatized 38 keV x-rays without focusing are introduced to the experimental hutch through the vacuum path from the optical hutch and used as an incident beam. The scattered x-rays were detected with a imaging plate of 300 mm × 300 mm located about 3 m apart from the sample position. A vacuum path is mounted between the sample and the imaging plate. Using a lead beam stopper, 5 mm × 5 mm, the observable wavenumber k ($k = 4\pi \sin\theta/\lambda$; λ: wavelength) is estimated to be from 0.02 Å^{-1} to 0.9 Å^{-1}. The details of the beamline are given elsewhere [21].

High-pressure apparatuses similar to those for the x-ray diffraction experiment are installed in the experimental hutch. A side view of the high-pressure vessel for the SAXS measurement is shown in figure 7. A synthetic diamond 3 mm in diameter and 3 mm in thickness of the highest quality is used as a window for an incident beam instead of Be, which is known to generate a large parasitic scattering. For scattered x-rays, a Be window 10 mm in diameter is chosen to observe the spectrum up to larger scattering angle. The designs of the sapphire cell and the heating accessories are the same as those for the x-ray diffraction experiments, except that the cell is made of a polycrystalline sapphire and there is a Mo tube without a slit. There is no parasitic scattering from the polycrystalline sapphire in the observed k-region even at high temperatures. W–26% Re:W–5% Re thermocouples were used instead of Pt–Rh thermocouples because temperatures higher than 1650 °C had to be measured for fluid Se.

In a typical measurement, the intensity of transmitted x-rays was first monitored using an ionization chamber with Ar gas just in front of the imaging plate to carry out an absorption correction. Then the chamber was removed and the imaging plate was exposed for five minutes after an erasing procedure. Figure 8 shows the intensity spectra of an empty cell (solid line) and the cell and fluid Se near the critical density (dots and line) after absorption correction. The inset shows the smaller-intensity region on an enlarged scale. The large background intensity from 0.02 Å^{-1} to 0.08 Å^{-1} arises from the Be window of the high-pressure vessel. After deducing the small-angle scattering spectrum by subtracting the intensity of the empty cell, a reliable k-minimum is found: it is around 0.06 Å^{-1}. A small peak which comes from a Kapton window of the vacuum path is observed at around 0.37 Å^{-1}. The smaller maximum k of 0.4 Å^{-1} comes from the geometrical constraint of the diameter of the Be window.
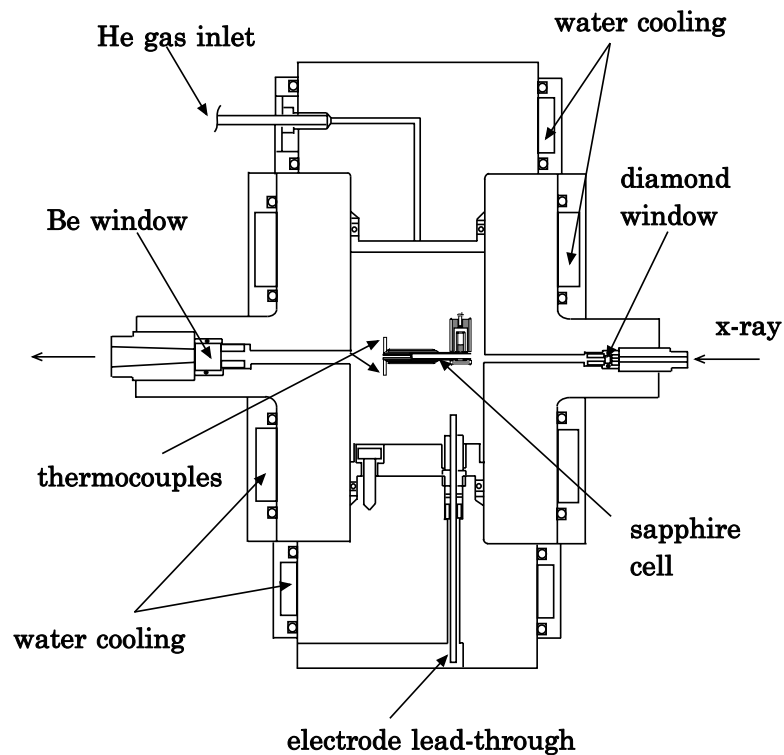
Figure 7. A side view of the high-pressure vessel for SAXS measurements.
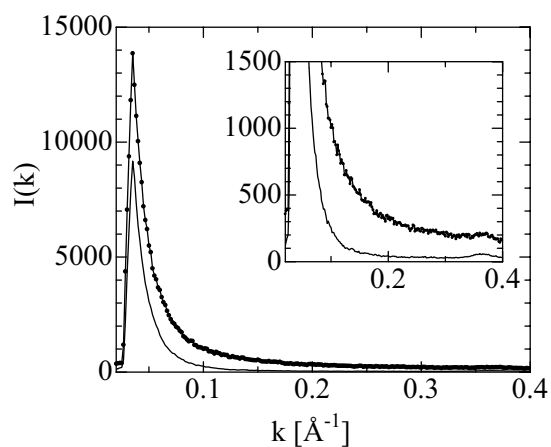

Figure 8. SAXS intensity spectra of an empty cell (solid line) at 25 °C and the cell and fluid Se at 1680 °C and 457 bar near the critical density (dots and line) after absorption correction. The inset shows the smaller-intensity region on an enlarged scale.

2.3. XAFS measurements

XAFS measurements around the Se K edge for fluid Se were carried out in transmission mode using the spectrometer installed by the French Collaborative Research Group on the BM32

beamline at the ESRF. The storage ring was operated at 6 GeV in the multibunch mode with a 200 mA current. The beamline optics incorporates a Si(111) double-crystal monochromator, with an axis angular resolution of 1×10^{-4} rad. The horizontal focusing of the beam fan is performed by sagittally and dynamically bending the second crystal of the monochromator. The vertical focusing is obtained using a Ni-coated mirror installed upstream. The beam size at focus is about 0.3 mm $\times$ 0.3 mm. The intensities I_0 and I of the incident and transmitted beams were monitored through measurement of the intensities scattered by a Kapton foil. Each measurement is performed using two Si diodes located above and below the x-ray beam to compensate for any slight motion of the focused beam during the energy scan. The details of the optics are given in the earlier paper [22].

The experimental conditions of high temperature and high pressure were achieved using an internally heated high-pressure vessel made of super-high-tension steel similar to the previous one [23, 24]. Figure 9 shows a side view of the high-pressure vessel. The incident and transmitted x-ray beams pass through Be windows of 5 mm thickness and 4 mm diameter. The vessel is pressurized by He gas of high-purity grade (99.9999%). The pressure is measured with absolute pressure transducers, having an accuracy of $\pm 0.3\%$ full scale, which can be used up to 700 bar. The vessel is cooled with water flowing through jackets placed around its outside.
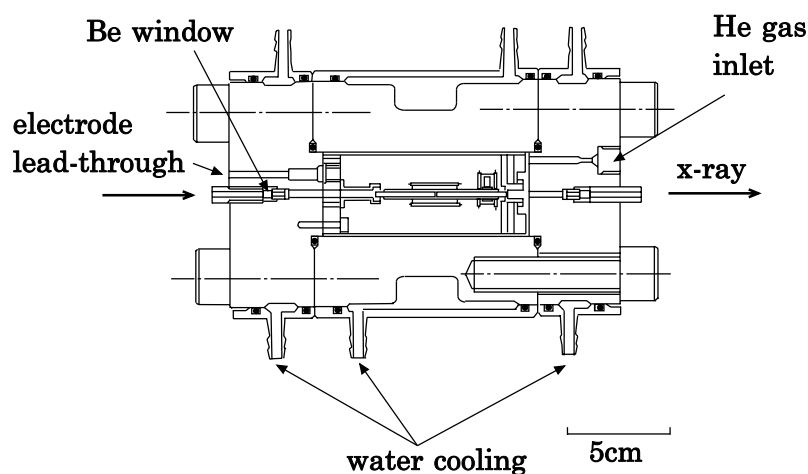

Figure 9. A side view of the high-pressure vessel for XAFS measurements.

The high-purity-grade (99.999%) Se sample is contained in a cell made of polycrystalline sapphire which is resistant to chemical reaction with Se at high temperatures. The cell is located in the centre of the vessel. Figure 10 shows the cell and heating accessories. The cell consists of a hot area and a sample reservoir like the cell used for the scattering experiments. A closed-end polycrystalline sapphire tube with an inner diameter of 2.0 mm and an outer diameter of 3.0 mm was placed in another tube with an inner diameter of 3.0 mm and an outer diameter of 4.5 mm. The sapphire components were connected with the high-temperature ceramic adhesive. The thickness of the closed end of each tube was 250 μm and the gap was fixed to give a suitable jump at the absorption edge. The sample thickness was chosen to be 30 μm for the measurements in the SC–M transition region, and 50 μm from the metallic fluid to the dense vapour near the critical density. The thickness of 100 μm was used for the measurements of dense Se vapour with densities smaller than the critical density. The temperature was measured at three locations by Pt–30% Rh:Pt–6% Rh thermocouples and the
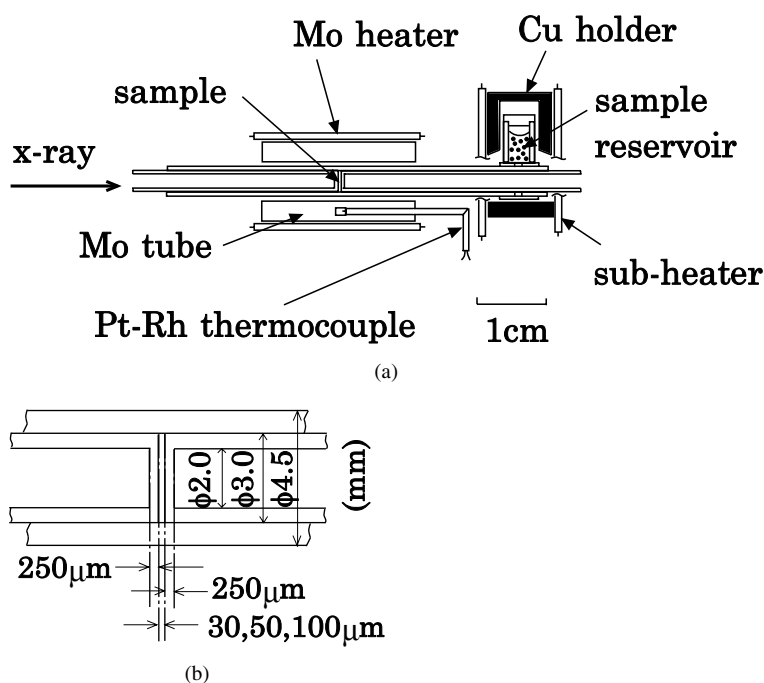
Figure 10. (a) The construction of the sapphire cell used for the present XAFS experiments. (b) Details of the sample space shown on an enlarged scale.

difference of the temperatures was within 5 °C at 1650 °C. After liquid Se was loaded in the thin space of the cell at 500 °C and 1 bar, the vessel was pressurized up to 600 bar. Then we increased and controlled the temperature to measure the XAFS spectra. Near the critical density, ρ_c, the pressure was decreased at intervals of 4 bar and the spectra were measured at each pressure.

3. Structural changes in fluid mercury

3.1. M–NM transition in fluid mercury

Liquid Hg is transformed into an insulating state when it is expanded to the liquid–gas critical point (critical data of Hg [25]: $T_c = 1478$ °C, $p_c = 1673$ bar, $d_c = 5.8$ g cm^{-3}). Figure 11 shows the density isochores plotted in the pressure–temperature plane [25]. A bold solid line indicates the saturated-vapour-pressure curve and the cross shows the critical point. Many investigations have been made focusing on the M–NM transition in fluid Hg. The first indication of the M–NM transition was found in the electrical conductivity and thermopower data obtained by Hensel and Frank [1]. Measurements of physical properties such as electrical conductivity [26–28], thermopower [26, 29–31], Hall coefficient [32], optical reflectivity [33, 34], optical absorption coefficient [35, 36] and nuclear magnetic resonance [37] indicate that, as the density is reduced, the M–NM transition starts to occur at a density of about 9 g cm^{-3}.

Theoretical attempts have been made to understand the M–NM transition. Devillers and Ross [38] applied a pseudopotential method to calculate the energy bands for crystalline Hg with expanded bcc, fcc and rhombohedral structures. Band-structure calculations for such a uniformly expanded crystalline Hg were carried out by many others [39, 40]. An alternative
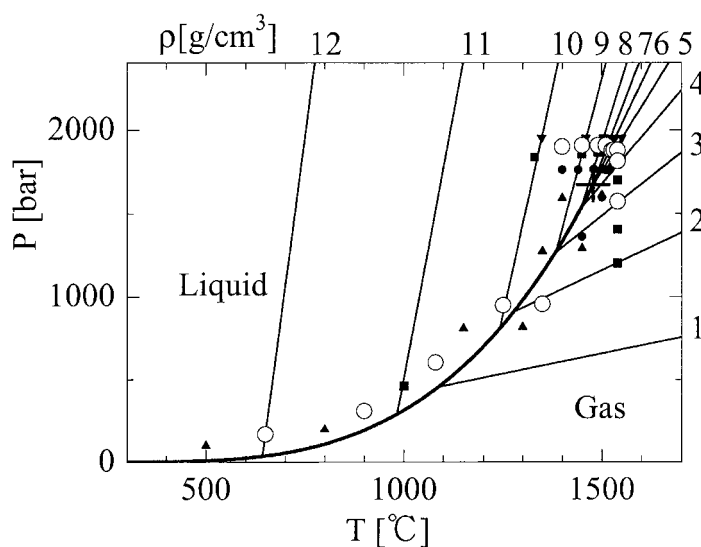
Figure 11. The density isochores for fluid Hg plotted in the pressure–temperature plane [25]. A bold solid line indicates the saturated-vapour-pressure curve and the cross shows the critical point. Open circles show the pressures and temperatures at which x-ray diffraction measurements were performed using the new high-pressure vessel with seven windows. The sample thickness is 50 μm. Solid symbols denote the points measured using the old high-pressure vessel. The sample thicknesses are 30 μm (triangles), 60 μm (circles), 80 μm (downward-pointing triangles) and 120 μm (squares).

approach taken by Mattheis and Warren [41] assumed that the nearest-neighbour distance was constant, and hence that the density variation in expanded fluid Hg was due entirely to the changes in the coordination number.

It is obvious that information on the atomic arrangement of expanded fluid Hg is quite important for the understanding of the M–NM transition. However, diffraction experiments for expanded fluid Hg are not easy to carry out because the critical pressure is very high. Recently Tamura and Hosokawa measured x-ray diffraction using an in-house x-ray source for expanded liquid Hg in the metallic region and also up to the critical region [3–5]. They obtained information about the first-neighbour coordination: the first-neighbour distance, r_1, remains almost constant while the first-neighbouring coordination number, N_1, decreases substantially and almost linearly with decreasing density in the metallic region.

3.2. Experimental results

We have carried out x-ray diffraction measurements at SPring-8 for expanded fluid Hg in the temperature and pressure ranges to 1540 °C and 1908 bar along the saturated-vapour-pressure curve and with densities ranging from 13.6 to 1.9 g cm^{-3} using the new high-pressure vessel. The measured points are indicated in figure 11 by open circles. The details of the experiments will be described elsewhere. The figure also shows the points measured with the old high-pressure vessel, as closed symbols. The main parts of these results have been published elsewhere [14]. Figure 12 shows $S(k)$ for expanded fluid Hg at the different temperatures and pressures obtained using the new vessel and the cell with the sample thickness of 50 μm. Dots represent the experimental data and the full curves show the Fourier transforms of the $g(r)$ from figure 13.
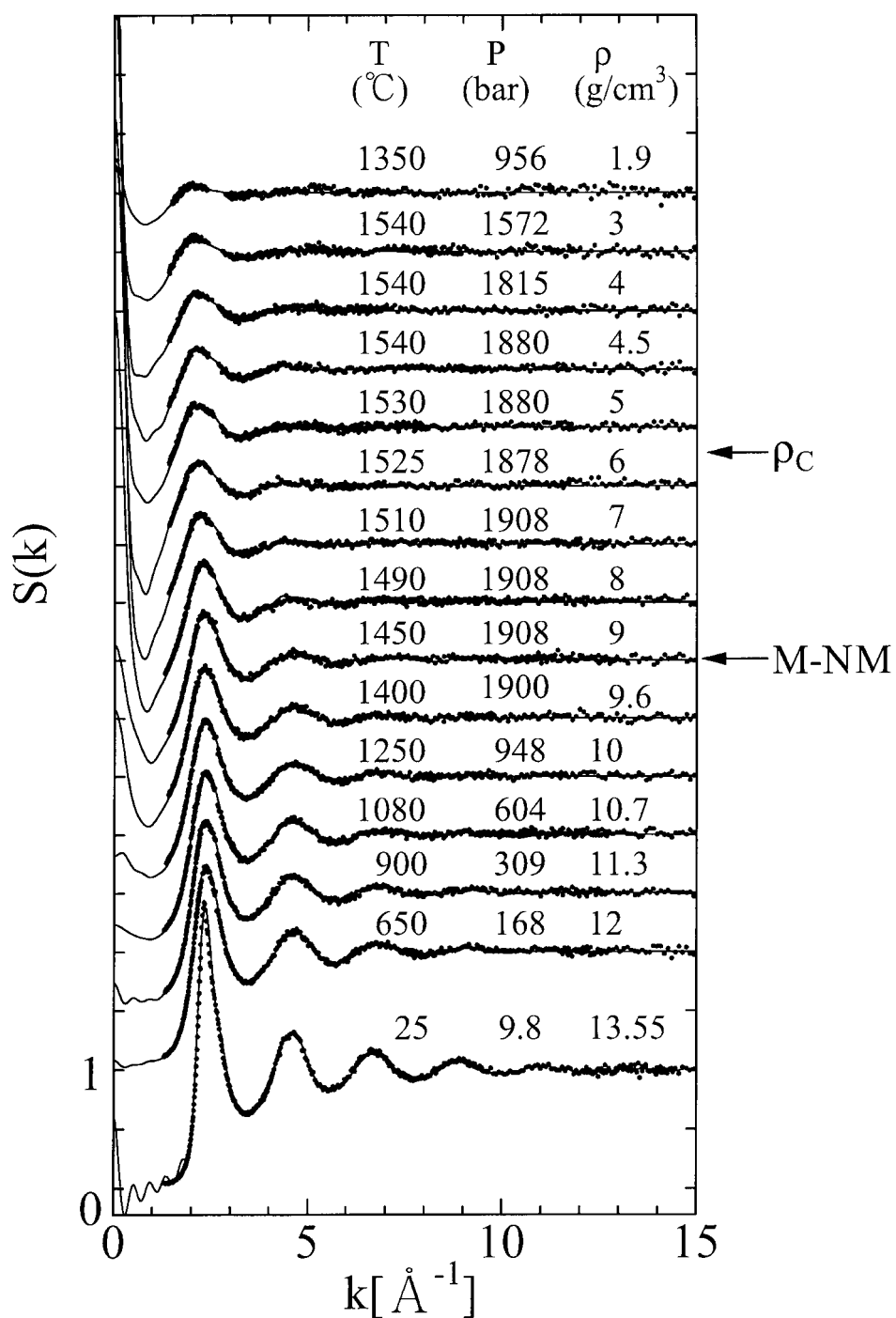
Figure 12. Structure factors $S(k)$ for expanded fluid Hg at the temperatures and pressures denoted by open circles in figure 10. The temperature and pressure range up to 1540 °C and 1908 bar along the saturated-vapour-pressure curve. Temperature, pressure and density are indicated at the upper right-hand side of each of the sets of data points. The dots represent the experimental data and the full curves show the Fourier transforms of the the $g(r)$ from figure 13.
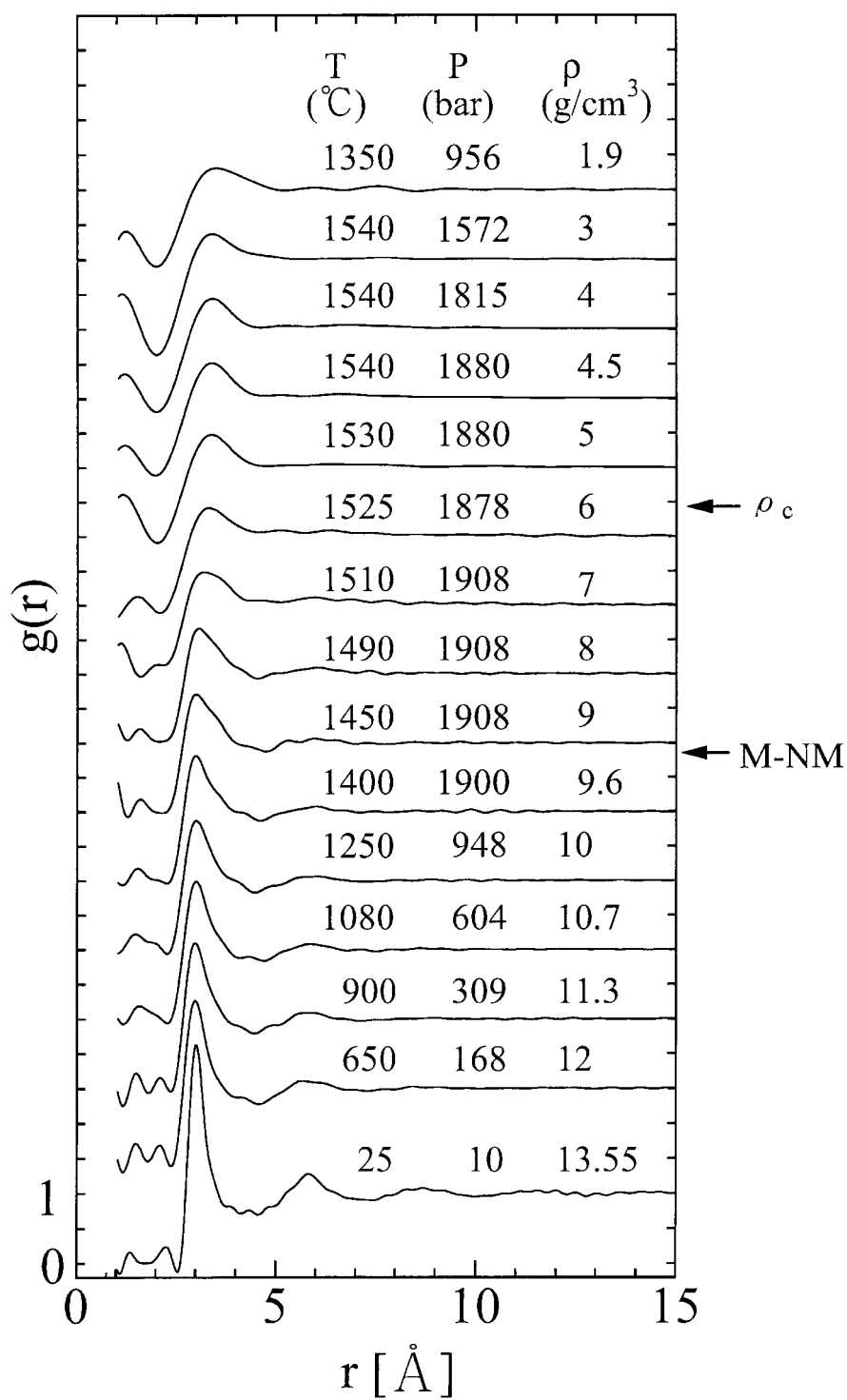
Figure 13. Pair distribution functions $g(r)$ for expanded fluid Hg. Temperature, pressure and density are indicated at the upper right-hand side of each of the data curves.

Figure 13 shows the $g(r)$, the Fourier transforms of the $S(k)$ for fluid Hg shown in figure 12. The transformation of the $S(k)$ function requires data from $k = 0$ to ∞. The $S(k)$s in the region between 0 and 1.0 Å^{-1} were estimated by interpolating the $S(0)$s and $S(k)$ above 1.0 Å^{-1}, where the $S(0)$s were calculated using the experimentally obtained isothermal compressibility of expanded fluid Hg [25, 27].

The data for $g(r)$ at 25 °C and 10 bar have several features: the first peak has an asymmetric shape, the first minimum is invariant in the region from 4 to 5 Å and the second peak is rather small. The data for $g(r)$ at 25 °C and 10 bar are in agreement with the previous data obtained under normal conditions [42]. With increasing temperature and pressure, with decreasing density, the long-range oscillation of $g(r)$ diminishes. A broadening of the first peak occurs gradually but no change of the peak position is observed and the asymmetry of the first peak remains even at temperatures and pressures up to 1490 °C and 1908 bar, respectively, with a density of 8.0 g cm^{-3}. It should be noted that the shape and the position of first peak change when the density decreases further and the dense vapour region is approached. The amplitude of the second peak decreases with increasing temperature and pressure.

3.3. Volume expansion, density fluctuation and M–NM transition

To obtain a definite coordination number, from the diffusive and broad $g(r)$ pattern of the non-crystalline state, we employed two different methods to define and to integrate the first-neighbour peak. The first one (method A) is the method of integrating $4\pi r^2 \rho_0 g(r)$ up to the maximum position of $g(r)$, r_1, and taking twice the integral, where ρ_0 denotes the average number density of Hg. The second one (method B) is a method of integrating $4\pi r^2 \rho_0 g(r)$ up to the first-minimum position of $g(r)$, r_{min}. We fixed r_{min} as 4.5 Å for the whole density range because r_{min} does not change so much except in the dense vapour region.

The coordination numbers N_A and N_B obtained by methods A and B, respectively, are plotted in figure 14 as functions of density. The nearest-neighbour distance r_1 is also shown as a function of density at the bottom of figure 14. Open circles show the present results and closed symbols show the results obtained using the old high-pressure vessel. As is seen in figure 14, N_B decreases substantially and linearly with decreasing density over a wide region from liquid to dense vapour. On the other hand, N_A also decreases almost linearly with decreasing density in the metallic region, but when the M–NM transition region is approached, i.e., around 9–10 g cm^{-3}, the deviation from the linear dependence emerges. It should be noted that the density around which the deviation starts to occur coincides with the region where the M–NM transition starts to occur. In contrast, no anomalous behaviour is observed in the behaviour of N_B around this density region. In the dense vapour region the density variation of N_A changes again. As seen in the figure, r_1 in the metallic region remains almost unchanged with decreasing density, but when the M–NM transition region is approached, r_1 starts to slightly increase. Such behaviour coincides with that of N_A. In the dense vapour region, r_1 substantially increases. The value of r_1 seems close to the interatomic distance of a Hg dimer in the rarefied vapour [44]. From these results we can conclude that the density decrease of fluid Hg is essentially caused by the reduction of the coordination number through the whole density region as seen in the behaviour of N_B. The volume expansion of liquid Hg in the metallic region is not a uniform expansion with a fixed coordination number, but is caused by a decrease of coordination number with a fixed nearest-neighbour distance as illustrated in figure 15(b). The atomic arrangement of metallic liquid Hg would be changed with decreasing density essentially according to the way in which the Hg atoms are taken away, one by one, from the random array with a constant nearest-neighbour distance. The variation of N_A, in contrast, gives more detailed information about the structural change accompanied by the M–NM transition. N_A
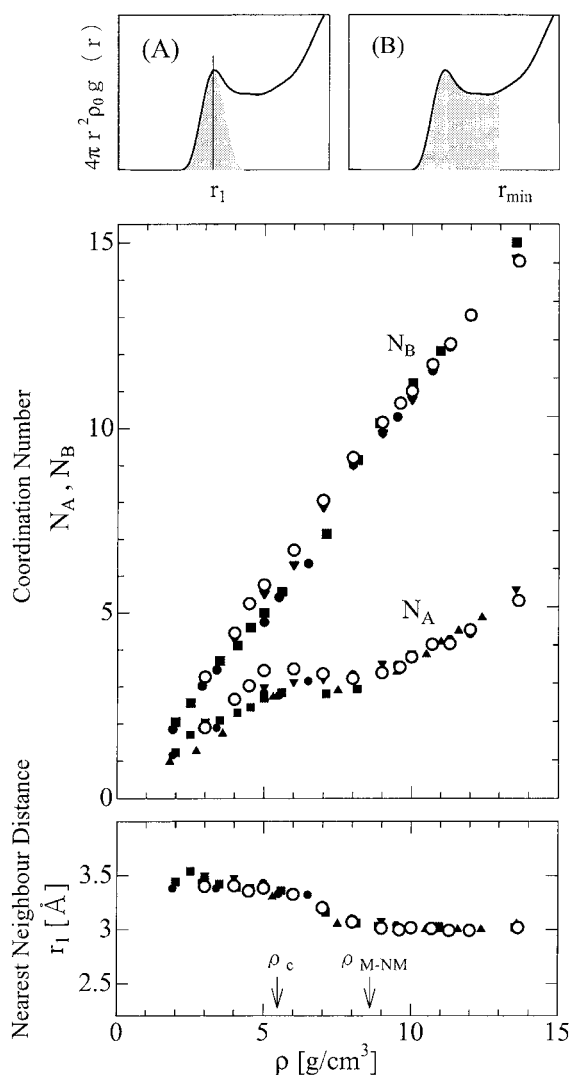
Figure 14. The coordination numbers N_A, N_B and the nearest-neighbour distance r_1 of expanded fluid Hg as functions of density. N_A and N_B are obtained using methods A and B, respectively (see the text). Open circles show the present data obtained using the new high-pressure vessel and the cell with the sample thickness of 50 μm. Closed triangles, circles, downward-pointing triangles and squares indicate the data obtained using the old vessel and the cells with the sample thicknesses of 30, 60, 80 and 120 μm, respectively.

represents the coordination number at the shortest distance in the first coordination shell, so the density variation of N_A suggests that the change of the nearest part of the first coordination shell is strongly related to the M–NM transition. Recently Nield and Verronen [46] and Arai and McGreevy [47] applied the reverse Monte Carlo modelling technique to the x-ray diffraction data for expanded fluid Hg using an in-house x-ray source [5]. They analysed the first coordination shell in detail and pointed out that knowledge of the variation of the near neighbours at shorter and longer distance in the first coordination shell is important to the understanding of the nature of the M–NM transition.
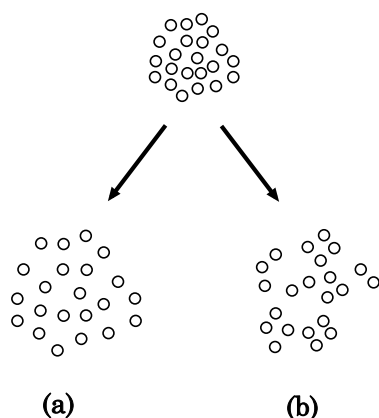
Figure 15. Schematic drawings of how the structural change of fluid Hg takes place in the microscopic sense with volume expansion: (a) a uniform expansion in which the nearest-neighbour distance, r_1, increases and the coordination number, N_1, remains constant and (b) an inhomogeneous expansion in which r_1 remains constant and N_1 decreases.

As mentioned in the previous section, several band-structure calculations were carried out for the hypothetical forms of crystalline Hg. One of the approaches whose principle was consistent with the present experimental results was that of Mattheis and Warren [41]. They assumed that the nearest-neighbour distance was constant, and hence that the density variation in expanded fluid Hg was due entirely to the changes in the coordination number. They performed a series of augmented-plane-wave calculations for crystalline Hg with fcc, bcc, sc and diamond structures with a fixed nearest-neighbour distance. They found that the trend of the density dependence of the theoretically calculated density of states (DOS) with the character of the 6s wave function is in good agreement with that of the Knight shift in the density range down to about 9.5 g cm^{-3} by assuming that N_1 for liquid Hg near the triple point was 10, and decreased linearly with decreasing density. However, their hypothetical crystal with diamond structure with $N_1 = 4$, which corresponds to $\rho = 5.4$ g cm^{-3} according to the interpretation of Warren and Hensel [45] using revised density data, indicates a semimetallic DOS, and it was found necessary to increase the lattice constant by 1% to fully open a gap.

Franz [48] proposed a model that produces a real gap at the correct density of 9 g cm^{-3}. The model was also based on the assumption of a linear decrease in average coordination number with decreasing density, but in addition it takes into account the fact that the actual local coordination numbers would be distributed randomly over a range around the mean N_1. It was assumed from the previous calculations [41] that for $N_1 = 4$ a gap is just about to open, while for $N_1 = 3$ a gap should exist. Franz postulated that the local gap of atoms with $N_1 = 3$ prevents electrons from hopping onto it from neighbouring atoms, and such a vacancy preventing transport propagates throughout the liquid at a well-defined mean density, creating a real gap in the total DOS. The density of the percolation threshold or the M–NM transition density obtained was about 9 g cm^{-3}. The results based on the model suggest that fluctuations of the coordination number affect the M–NM transition in fluid Hg.

Recently, Kresse and Hafner [49] made a theoretical investigation of the density variation of the structural and electronic properties of fluid Hg using an *ab initio* density-functional molecular-dynamics method. They found that a single-particle gap between the 6s and 6p bands opens at a density of about 8.8 g cm^{-3}. They were able to reproduce well the volume expansion in fluid Hg, which results not in an increase of the mean interatomic distance, r_1,

but in a decrease of the average coordination number, N_1. In addition, the asymmetry of the first peak in $g(r)$ was reproduced in their calculated results over the whole density range.

We have concentrated so far on discussing the density variation of the first-neighbour coordination. The most important remark on the present studies is as follows. First, fluid Hg expands, decreasing the coordination number. Second, the changes in the near neighbours at shorter distance in the first coordination shell must be important for the M–NM transition. Third, as seen in the density variation of N_A and r_1 in figure 14, there exist three different regions in the density, that is, the metallic region from 13.6 to about 10 g cm^{-3}, the M–NM transition region from 10 to the critical density of about 6 g cm^{-3} and the dense vapour region.

4. Structural changes in fluid selenium

4.1. SC–M–I transition in fluid selenium

Liquid Se, which behaves as a semiconductor near the melting point and has a twofold-coordinated chain structure where atoms are covalently bonded, experiences a semiconductor–metal–insulator transition around the critical point (critical data for Se [50]: $T_c = 1615\ °C$, $p_c = 385$ bar, $\rho_c = 1.85$ g cm^{-3}).

The first indication of the SC–M transition in fluid Se was found in electrical conductivity data obtained by Hoshino *et al* [51, 52]. Figure 16 shows the contours of constant dc conductivity plotted on the p–T plane [53, 54]. The high-conductivity region appears in the immediate vicinity of the critical point. Another indication was obtained from the measurement of the optical reflectivity by Seyer *et al* [55]. A Drude-like energy dependence of the reflectivity
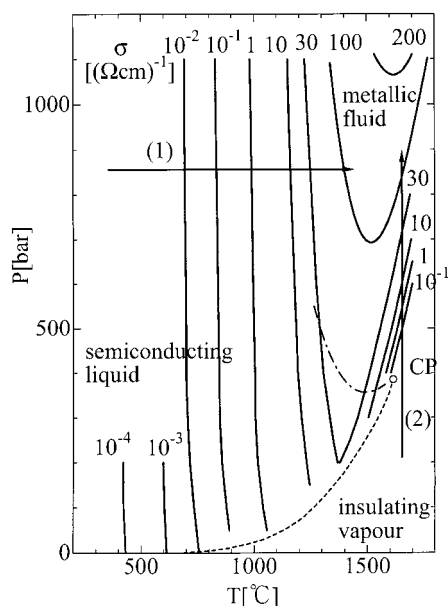

Figure 16. The contours of constant dc conductivity in liquid and supercritical fluid Se plotted in the pressure–temperature phase diagram. The illustration is taken from references [51, 53]. The broken curve is the saturated-vapour-pressure curve and the circle at the end denotes the critical point. The bold chain line indicates the location at which the optical gap of liquid Se disappears. See the text regarding arrows (1) and (2).

spectra was observed at elevated pressures and temperatures. Recent optical reflectivity measurements by Ikemoto *et al* [56] confirm the appearance of metallic behaviour near the critical point. Measurements of the optical absorption coefficient in the high-absorption range [57] have also shown that the region where the optical gap disappears is located near the critical point, as shown by the bold chain line in figure 16. From the measurements of viscosity [58], magnetic susceptibility [59] and NMR [54] near the melting point, an average chain length of 10^4–10^5 atoms may be estimated. At sufficiently high temperature and pressure, near the critical point, the average chain molecule contains only about ten atoms [54]. The characteristic features of the SC–M transition in fluid Se are as follows. First, the transition occurs with volume expansion. Second, the transition occurs when the chain length becomes very short and it seems to correlate with the instability of the chain structure. Arrow (1) shown in figure 16 denotes a typical process from the semiconducting liquid to the metallic fluid at high pressure.

A distinct behaviour accompanying the SC–M transition is also observed in the thermo-dynamic properties. The isochores start to bend at temperatures above 1100 °C and pressures above 400 bar [50, 60, 61] defining a contour of constant dc conductivity of 30 Ω^{-1} cm^{-1} in figure 16. The bending of isochores suggests the onset of a transition to a densely packed structure. It has been speculated that a large number of structural defects, such as threefold-coordinated centres in the branched chain, appear [60]. On the basis of the model proposed by Cabane and Friedel [62], neutral threefold-coordinated centres have been considered to play a crucial role in the mechanism of the appearance of the metallic state in fluid Se. It is obvious that structural data are important for the understanding of the mechanism of the SC–M transition in fluid Se. Edeling and Freyland [63] used neutron diffraction to investigate the static structure of liquid Se in the temperature range from 600 °C to 1400 °C at pressures up to 265 bar. Their data gave no indication of the existence of a significant concentration of threefold-coordinated sites.

When the metallic fluid is further expanded, the conductivity begins to decrease and the fluid finally becomes an insulating vapour consisting of Se dimers, which suggests that a metal–insulator (M–I) transition occurs in a further volume expansion process around the critical point. This fact raises another interesting question: that of how Se dimers condense to the metallic fluid consisting of chain molecules along arrow (2) shown in figure 16.

4.2. Structural changes in the SC–M transition

Figure 17(a) shows the most recent results on $S(k)$ for fluid Se from the semiconducting liquid near the melting temperature to the metallic fluid up to 1500 °C and 884 bar, obtained using the new high-pressure vessel. The figure includes $S(k)$ in the dense vapour phase at 1650 °C and at 392 bar, which was obtained for the first time. The details of the results will be described elsewhere. $S(k)$ below 1 Å^{-1} is interpolated to the $S(0)$ value estimated from the thermodynamic values of fluid Se. It is noticed that the phase of the oscillation in $S(k)$ around 8 Å^{-1} starts changing at 1000 °C as shown in figure 17(b).

The pair distribution function $g(r)$ obtained from Fourier transformation of $S(k)$ is shown in figure 18. The first peak in $g(r)$ corresponds to the distribution of the intrachain nearest-neighbour atoms. The first and second peaks are clearly separated in the semiconducting region. With increasing temperature these peaks become broad and the first minimum between them becomes high while the peaks are rather well separated even at 1500 °C. These new results on $g(r)$ obtained using the high-pressure vessel with seven windows show that the first peak is sharp and the asymmetric behaviour which we reported in the previous paper [70] is reduced in the metallic region, because the present $S(k)$s have oscillations in the larger-k region even
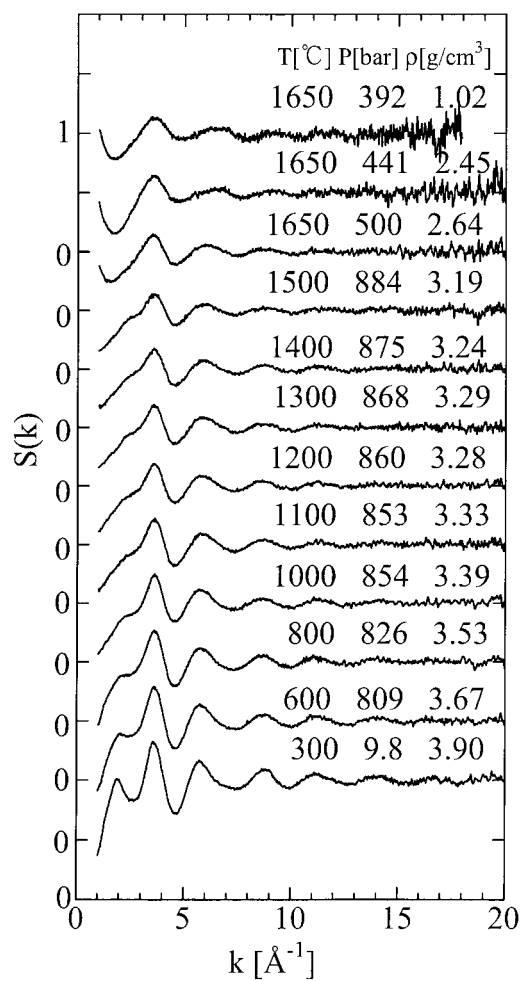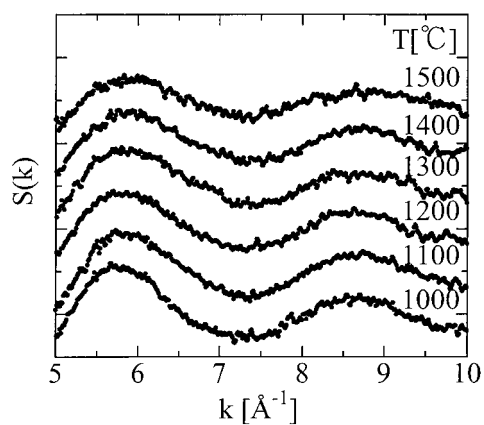
Figure 17. (a) $S(k)$ for fluid Se at various temperatures and pressures obtained using the new high-pressure vessel. (b) $S(k)$ data around 8 Å^{-1} from 1000 °C to 1500 °C on an enlarged scale.
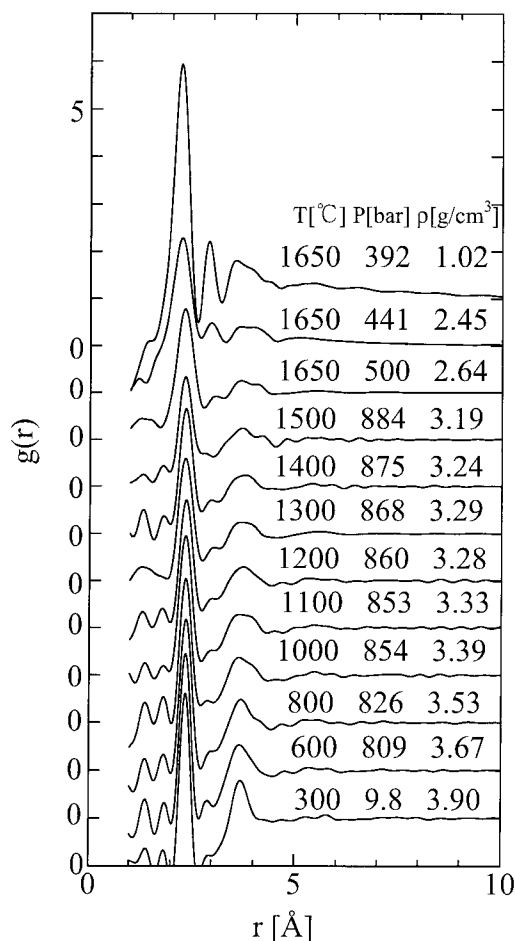
Figure 18. The $g(r)$s obtained from Fourier transformation of the $S(k)$s shown in figure 17.

at 1500 °C. To show the structural change in the SC–M transition, the nearest-neighbour distance r_1 and the coordination number N_1 of fluid Se are plotted in figure 19 as functions of temperature. To obtain a definite coordination number, we employed method A and method B defined in the previous section. The coordination numbers N_A and N_B obtained by methods A and B, respectively, are plotted in figure 19. Open symbols indicate the present results and closed symbols show ones obtained using the old high-pressure vessel [70]. As clearly shown in the figure, N_A and N_B remain about 2 in the measurement temperature and pressure region and decrease slightly with increasing temperature. Most importantly, the twofold-coordinated structure is largely preserved even in the metallic region above 1300 °C. The value of r_1 also barely changes and decreases slightly with increasing temperature.

The XAFS technique is useful for getting information on the local atomic arrangement of a material. We have carried out XAFS measurements for fluid Se up to the supercritical region [22]. Figure 20 shows XAFS spectra, $\chi(k)$, of fluid Se at different temperatures at 600 bar. It should be noted that the oscillation is damped with increasing temperature but can be seen even at 1650 °C. This suggests that a covalent bond still exists at such high temperatures. From a curve-fitting analysis based on a one-Gaussian model, the temperature variation of r_1
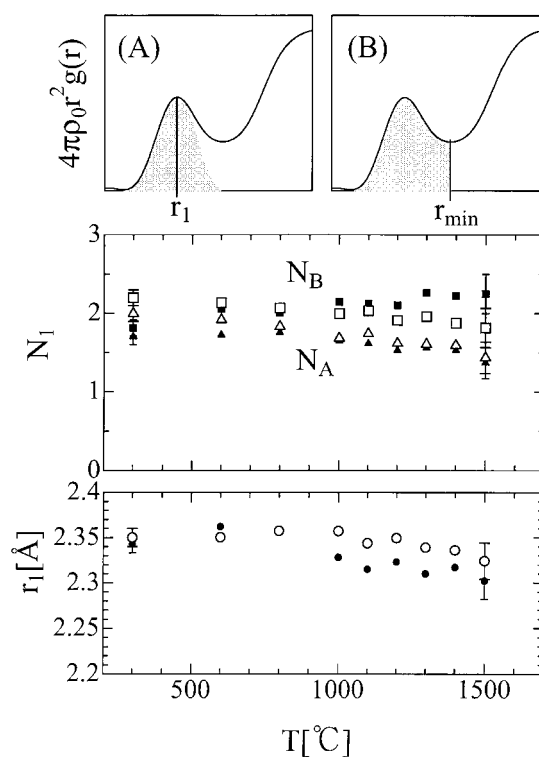
Figure 19. The coordination numbers N_A (triangles), N_B (squares) and the nearest-neighbour distance r_1 (circles) for expanded fluid Se as functions of temperature. N_A and N_B are obtained using methods A and B, respectively (see the text). Open symbols indicate the present results and closed symbols show the data obtained using the old high-pressure vessel [70].

is obtained and the results are shown in figure 21. The value of r_1 is almost constant in the semiconducting region and clearly decreases around 1200 °C, which is consistent with the results of the x-ray diffraction measurements.

4.3. The origin of the SC–M transition

The crystal structure of Se can be well understood using the schematic diagram shown in figure 22; the helical chain structure is matched with the cube edges, giving an average orientation along the (1, 1, 1) direction, and the observed structure is obtained by a slight distortion [64, 65]. The electronic configuration of atomic Se is $4s^2 4p^4$. The two s electrons are sufficiently low in energy that they do not participate in bonding. Two p electrons form covalent σ-bonds and the remaining two p electrons enter the non-bonding lone-pair (LP) state. The LP states are the highest filled states and form the valence band, while empty anti-bonding σ^*-states form the conduction bands shown in figure 22. Hence trigonal Se behaves as a semiconductor. As seen in the figure, the doubly occupied LP orbitals are located along the chain, and adjacent LP orbitals are orthogonalized to each other. The highest occupied LP orbital faces a lowest unoccupied anti-bonding orbital in the adjacent chain, which may cause the tendency toward charge transfer from the LP to the σ^*-state and the creation of a new bond between chains when the interchain distance is reduced. Since the twofold-coordinated structure in the crystalline Se is largely preserved upon melting, the characteristic features of
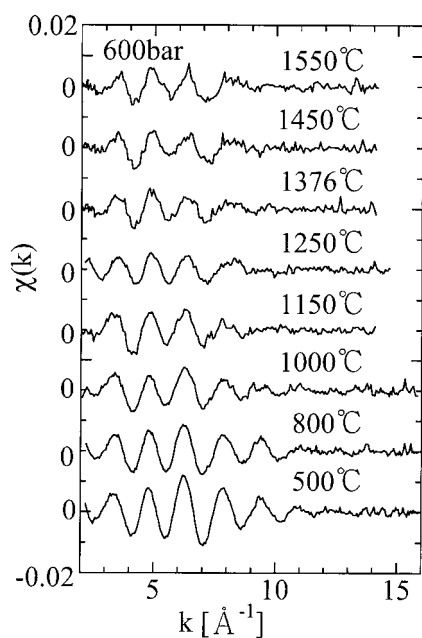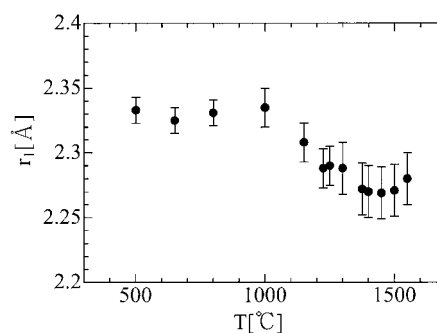
Figure 20. XAFS spectra, $\chi(k)$, of fluid Se.

Figure 21. Temperature variation of r_1 at 600 bar obtained from the curve-fit analysis of $\chi(k)$.
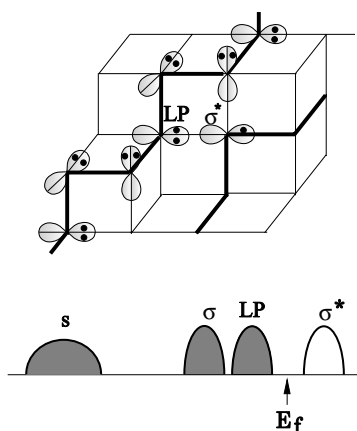

Figure 22. Schematic illustrations of the structure and electronic configuration of crystalline Se [64, 65] together with the density of states.

the structural and electronic properties of liquid Se near the melting point are essentially the same as those in the crystalline state.

To explain the SC–M transition it has been speculated [60] that threefold-coordinated sites are created in branched chains. The neutral threefold-coordinated centres are of special interest because their electronic configuration produces one conduction electron as shown in figure 23 [62]. The transition to the metallic state has long been believed to be induced by the progressive increase in the number of neutral threefold defects. Such a speculation is consistent with the tendency towards a new interchain bonding as shown in figure 22.
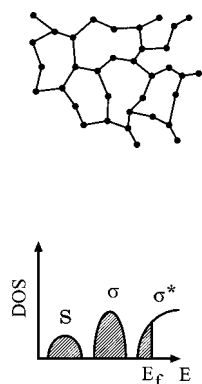
Figure 23. Schematic illustrations of the structure of threefold-coordinated centres and its density of states (DOS).

However, the present structural data give no clear indication of the existence of threefold-coordinated centres in fluid Se up to the temperature and pressure region of interest. We have found that the twofold-coordinated structure is largely preserved in the region where the optical gap disappears, and the conductivity becomes large, exceeding $200 \, \Omega^{-1} \, \text{cm}^{-1}$ [10]. An explanation for the structural change accompanying the SC–M transition should be proposed on the basis of the experimental facts.

Recently Ohtani *et al* [66] introduced structural models for expanded Se and calculated the electronic states and wave functions by a simulated annealing method. They have clearly shown that when some of the Se–Se bonds in the 'helical chain' are weakened in the process of expansion, the splitting between the bonding and anti-bonding levels is reduced and consequently the anti-bonding band is relatively lowered, which leads to the disappearance of the band gap between the anti-bonding and lone-pair band. They pointed out, furthermore, that the mechanism of the SC–M transition in fluid Se accompanying the volume expansion is completely new and different from those of the case of the non-metal–metal transition occurring with the volume reduction, such as the Wilson transition induced by the band overlap or the Mott transition relating to the change of the electron correlation. Shimojo *et al* [67] investigated the SC–M transition in fluid Se by means of an *ab initio* molecular-dynamics simulation. They found that the chain-like structure persists even in the metallic state, although the chain structure is substantially disrupted. By means of a detailed investigation of the time change of the chain structure they have shown that the interaction between the Se chains is important for bond breaking, and that bond breaking and rearrangement of the Se chains occur more frequently at higher temperatures. They pointed out that when the Se–Se bonds break, the anti-bonding states above the Fermi level E_F are stabilized while bonding or non-bonding states below E_F become unstable, and, therefore, the gap at E_F disappears at high temperatures. Kirchhoff *et al* [68] also performed an *ab initio* simulation for fluid Se and obtained results almost consistent with those of Shimojo *et al* [67]. These theoretical studies have clearly shown the possibility that the SC–M transition in expanded fluid Se may occur retaining the twofold-coordinated structure with bond breaking. In spite of these works, however, there still exists the idea that threefold-coordinated sites are important for the SC–M transition. Bichara *et al* [69] investigated the structure of liquid Se by means of a Monte Carlo simulation using the semi-empirical model based on a tight-binding approximation and asserted that the fraction of onefold- and threefold-coordinated atoms which play a crucial role in the SC–M transition increases at high temperatures.

Our new result that the asymmetric distribution in $g(r)$ for the metallic fluid becomes small compared with the previous ones [70] may suggest the revival of our previous model. According to theoretical studies [71] on an isolated Se chain with a wide range of geometry, a Se chain with infinite length is reported to have the electronic conformation with overlapping of the valence and conduction bands in the planar zigzag geometry. In the semiconductor region, a helical chain structure similar to that of crystalline Se is considered to be stable while the sign of the dihedral angle along the chain should be randomly distributed in the liquid state. At higher temperature, LP electrons are thermally excited to the conduction band and the exchange repulsion of LP electrons, which plays an important role in stabilizing the dihedral angle near 90°, is reduced. As a result, there is a possibility that the chain changes from the helical conformation to the planar zigzag one. The planar zigzag conformation may easily be stabilized in the very short chain at high temperature because the effect of the excitation of a LP electron and the effect of the chain ends may easily extend over the short chain, as shown in figure 24. As a result of formation of a π-bond in addition to a σ-bond, the bond in the zigzag chain becomes strong and short, which is consistent with the experimental results. The metallic behaviour of fluid Se with twofold-coordinated structure may be attributed to a short chain molecule with the planar zigzag conformation.
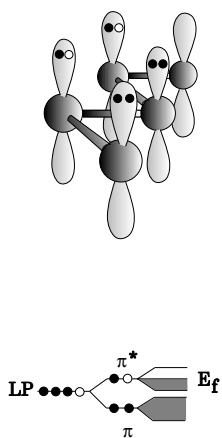

Figure 24. Schematic illustrations of the structure and the electronic states of the chain molecule with the planar zigzag conformation.

4.4. Structural changes from rarefied vapour to metallic fluid

To investigate the density variation of the intrachain covalent bonds, XAFS measurements have been carried out at 1650 °C in the density region from dense Se vapour to supercritical fluid Se [72]. Figure 25 shows the radial distribution function, $|F(r)|$, obtained from Fourier transformation of $\chi(k)$. The density ρ is estimated from the x-ray absorbance. Note that these data were obtained in the insulating region where the dc conductivities are less than 10^{-1} Ω^{-1} cm^{-1}. The peak in $|F(r)|$ of 1.4 g cm^{-3} is symmetrical. The r_1 obtained from the curve-fit analysis is 2.18 Å, which suggests that most of the molecules in the fluid are Se dimers. When ρ exceeds $\rho_c = 1.85$ g cm^{-3}, the peak in $|F(r)|$ becomes asymmetrical toward larger r and the asymmetrical behaviour remains with increasing density up to 2.5 g cm^{-3} at 600 bar. We performed the curve-fit analysis on the basis of the two-Gaussian model for these asymmetrical peaks and the bond lengths obtained are 2.18 Å and 2.30 Å.
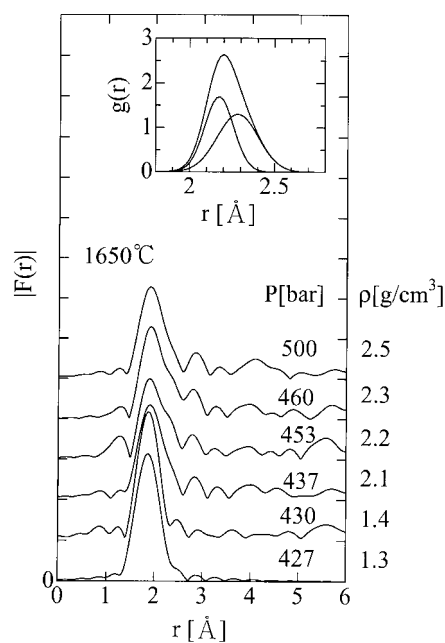
Figure 25. The radial distribution function, $|F(r)|$, of supercritical fluid Se near the critical point obtained from Fourier transformation of k times $\chi(k)$. The pair distribution function $g(r)$ reproduced using the optimized parameters for fluid Se at 500 bar is shown in the inset.

The length of 2.18 Å corresponds to that of a Se dimer. The length of 2.30 Å is close to that of metallic fluid Se. The $g(r)$s reproduced using the optimized parameters for fluid Se with the density of 2.5 g cm^{-3} are shown in the inset of the figure. These constitute the first evidence suggesting that the supercritical fluid in the *non-metallic* region with density greater than ρ_c is a mixture of Se dimers and other larger molecules related to the metallic fluid Se. This result may suggest that large density fluctuations near the isochore of ρ_c and the strong intermolecular interaction induce the formation of such larger molecules from Se dimers. The coordination numbers of dimers and chain molecules are optimized to 0.40 and 0.48, respectively, at 2.5 g cm^{-3}. Because it is said that the coordination number obtained from XAFS spectroscopy becomes smaller than the real one for a system with large disorder, the absolute values probably have a large error. However, we think that the ratio of the coordination numbers, which gives the weight of dimers and chain molecules, is more reliable than the actual values. When we assume that Se$_7$ chain molecules are dominant in the supercritical region as reported by Warren and Dupree [54], we can estimate from the ratio that the weight of the atoms which form the chain molecules is about 40%. This percentage seems to be within an expected range of values in spite of the large errors in the coordination numbers.

To investigate the density fluctuations near the critical point, we have carried out SAXS measurements for fluid Se using synchrotron radiation at SPring-8. Critical opalescence of fluid Se is observed for the first time. Figure 26 shows SAXS spectra at 1680 °C and at the pressures indicated in the figure. The absolute value of the intensity is estimated from the scattering intensity of compressed He gas and the scale of the ordinate is converted to the dimensionless structure factor, $S(k)$, according to our previous procedure [73]. In the present analysis, the scattering intensity of the compressed He gas is much smaller than the background intensity and the uncertainty of the estimated scaling factor may be several tens per cent.
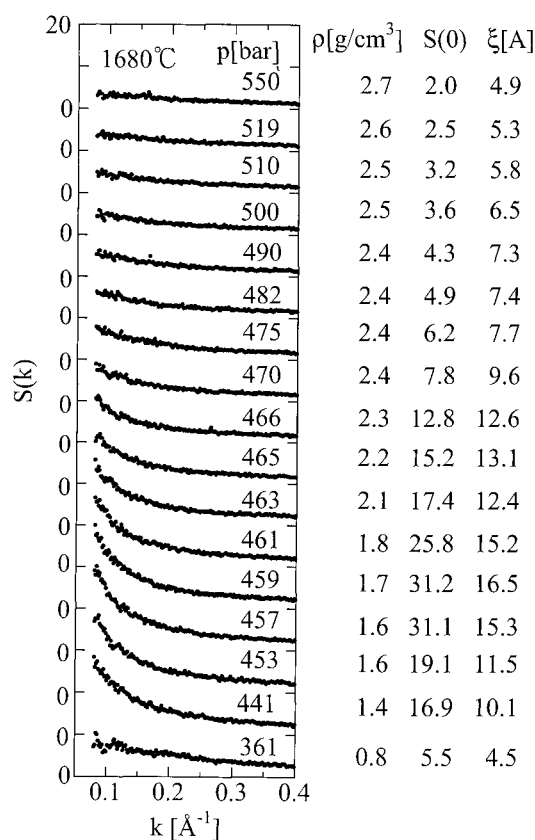
p[bar]	$\rho[g/cm^3]$	S(0)	$\xi[Å]$
550	2.7	2.0	4.9
519	2.6	2.5	5.3
510	2.5	3.2	5.8
500	2.5	3.6	6.5
490	2.4	4.3	7.3
482	2.4	4.9	7.4
475	2.4	6.2	7.7
470	2.4	7.8	9.6
466	2.3	12.8	12.6
465	2.2	15.2	13.1
463	2.1	17.4	12.4
461	1.8	25.8	15.2
459	1.7	31.2	16.5
457	1.6	31.1	15.3
453	1.6	19.1	11.5
441	1.4	16.9	10.1
361	0.8	5.5	4.5

Figure 26. SAXS spectra of fluid Se at 1680 °C. The scale of the ordinate is $S(k)$, which is estimated from the observed scattering intensity of compressed He gas. The density obtained from transmission measurements, $S(0)$ and ξ obtained from curve-fit analysis are shown in the figure.

From the detailed analysis using the Ornstein–Zernike equation:

$$S(k) = \frac{S(0)}{1 + \xi^2 k^2}$$

the correlation length, ξ, and the fluctuations of the number density,

$$S(0) = \frac{\langle (N - \langle N \rangle)^2 \rangle}{\langle N \rangle}$$

are deduced. The error of ξ is small because there is no correlation with the scaling factor of the ordinate. On the other hand, as the error of $S(0)$ is large, we confirm that the $S(0)$s obtained at 0.8 g cm^{-3} and 1.4 g cm^{-3} in the gaseous region are reasonable within the error. The details of the procedure will be described elsewhere.

In the critical region, ξ and $S(0)$ are obtained as 16.5 Å and 31, respectively, at 1.7 g cm^{-3} near the isochore of ρ_c. The results mean that the density fluctuations induce dense or rarefied regions with the average size of 16.5 Å in the fluid. Here you could imagine that, as an extreme picture, black and white cubes with a side length of 16.5 Å, which represent dense and rarefied regions respectively under the density fluctuations, arrange as a sodium chloride structure. The cube contains about 58 atoms at 1.7 g cm^{-3}, which means that the average number of Se dimers $\langle N \rangle$ is 29 and its fluctuation $\langle (N - \langle N \rangle) \rangle$ is estimated to be 21 from the observed $S(0)$.

As a result, the black cube contains 50 dimers and the density in the cube becomes 2.9 g cm^{-3}. The average distance between Se dimers is 4.5 Å at 2.9 g cm^{-3} while the distance is 5.4 Å at the average density of 1.7 g cm^{-3}. These results agree with the previous ones [73]. Chain molecules are expected to be formed in this dense state because of the strong intermolecular interaction between the dimers. Figure 27 is a schematic diagram of the configuration of dimers and chain molecules in dense and rarefied regions.
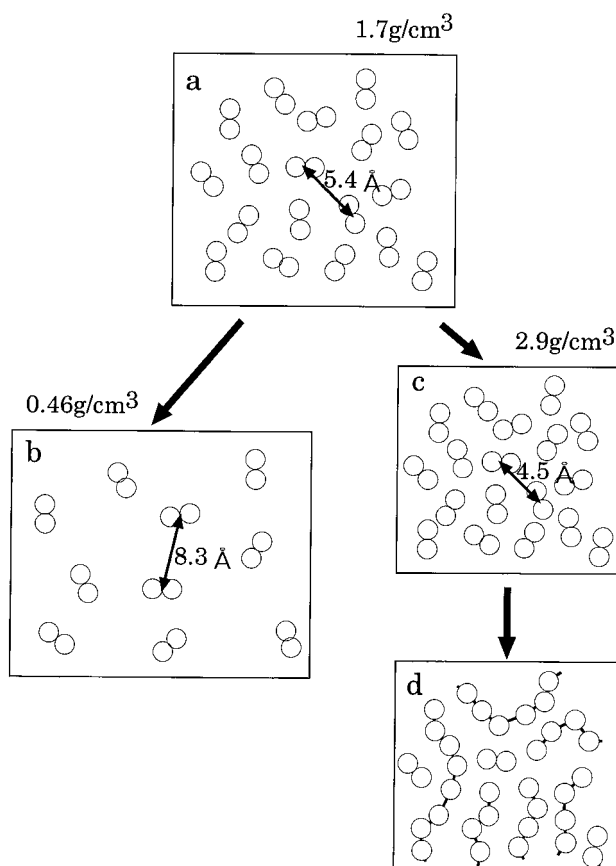

Figure 27. A schematic illustration of a snapshot of the atomic configuration of fluid Se under density fluctuations. (a) The average density of 1.7 g cm^{-3}, (b) a rarefied region and (c) a dense region under density fluctuations. (d) Chain molecules will be formed in the dense region.

An *ab initio* molecular-dynamics simulation was carried out by Shimojo *et al* [74] for fluid Se with the densities of 1 g cm^{-3} and 2 g cm^{-3} where spin effects were taken into account. The results show that in fluid Se at 1 g cm^{-3} most of the molecules are Se dimers while in that at 2 g cm^{-3} most of the Se atoms form chain molecules with metallic character. This result supports our speculation that chain molecules are formed in the dense state under the density fluctuations. Our XAFS results, however, indicate that fluid Se above the critical density is a mixture of Se dimers and chain molecules. This discrepancy between the experimental and simulation results may imply that the effect of the density fluctuations enhances the formation of Se dimers even in the density region above the critical density.

The results of the XAFS and SAXS measurements together with the simulation results give a picture of the structural change in the process of condensation of Se vapour into dense

fluid Se at a density exceeding ρ_c. The density fluctuations in the supercritical region near the critical point can induce the formation of chain molecules from Se dimers, where the chain molecules must be seeds of metallic fluid Se. So, the density fluctuation may induce fluctuations of the conductivity at a microscopic level. As seen in the pressure–temperature phase diagram of fluid Se shown in figure 28, the isochore of ρ_c is located below the contour of $0.1\ \Omega^{-1}\ \mathrm{cm}^{-1}$. Although fluid Se near ρ_c includes a seed of the metallic fluid, the average dc conductivity becomes insulating. It is speculated that when the region consisting of the chain molecules percolates over the whole fluid, the insulating fluid becomes metallic.
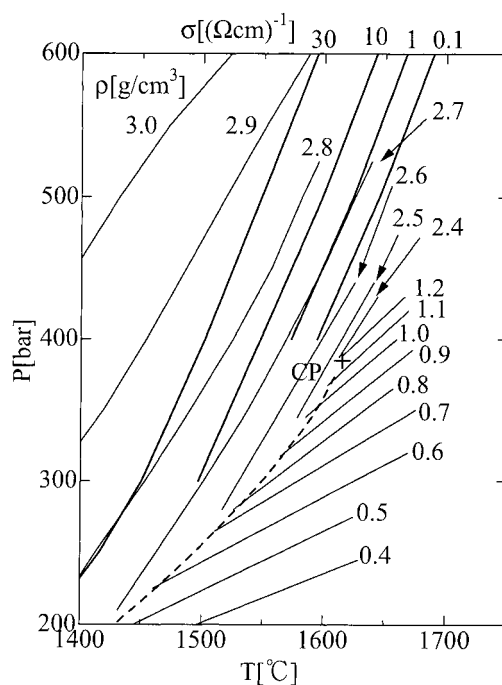

Figure 28. The contours of constant dc conductivity (bold line) in supercritical fluid Se [51, 53] near the critical point plotted in the pressure–temperature phase diagram. This illustration is taken from references [53, 54]. The thin solid lines denote the isochores of the fluid [50].

5. Summary

We have studied the structural changes relating to the M–NM transition in the supercritical fluids of Hg and Se using synchrotron radiation. Our results for fluid Se may be the first experimental evidence that the electronic properties are strongly correlated with density fluctuations in the critical region. To understand the structural and electronic properties of metallic fluids in the supercritical region, a quantitative value of the density fluctuations such as a correlation length is considered to be a more significant order parameter than its average density. In addition to the measurements presented here, inelastic x-ray scattering measurements for the supercritical metallic fluids will be carried out at SPring-8 to study a collective mode in the M–NM transition. In the near future, fruitful results should come from these experiments.

Acknowledgments

References

[1] Hensel F and Franck E U 1966 *Ber. Bunsenges. Phys. Chem.* **70** 1154
[2] Winter R, Bodensteiner T, Gläser W and Hensel F 1987 *Ber. Bunsenges. Phys. Chem.* **91** 1327
Franz G, Freyland W, Gläser W, Hensel F and Schneider E 1980 *J. Physique Coll.* C8 194
Winter R, Pilgrim C, Hensel F, Morkel C and Gläser W 1993 *J. Non-Cryst. Solids* **156–158** 9
[3] Hosokawa S, Matsuoka T and Tamura K 1991 *J. Phys.: Condens. Matter* **3** 4443
[4] Tamura K and Hosokawa S 1991 *J. Physique Coll.* IV C5 **1** 39
[5] Tamura K and Hosokawa S 1998 *Phys. Rev.* B **58** 9030
[6] Tamura K 1990 *J. Non-Cryst. Solids* **117+118** 450
[7] Tamura K and Hosokawa S 1992 *Ber. Bunsenges. Phys. Chem.* **96** 681
[8] Tamura K and Hosokawa S 1994 *J. Phys.: Condens. Matter* **6** A241
[9] Tamura K 1996 *J. Non-Cryst. Solids* **205–207** 239
[10] Inui M, Noda T and Tamura K 1996 *J. Non-Cryst. Solids* **205–207** 261
[11] Inui M, Noda T, Tamura K and Li C 1996 *J. Phys.: Condens. Matter* **8** 9347
[12] Tamura K, Inui M and Hosokawa S 1999 *Rev. Sci. Instrum.* **70** 144
[13] Tamura K, Inui M, Nakaso I, Oh'ishi Y, Funakoshi K and Utsumi W 1998 *J. Phys.: Condens. Matter* **10** 11 405
[14] Tamura K, Inui M, Nakaso I, Oh'ishi Y, Funakoshi K and Utsumi W 1999 *Japan. J. Appl. Phys.* **38** 452
[15] Tamura K, Inui M, Funakoshi K and Utsumi W 2001 *Proc. SRI2000* at press
[16] Nishikawa K and Iijima T 1984 *Bull. Chem. Soc. Japan* **57** 1750
[17] Cromer D T 1969 *J. Chem. Phys.* **50** 4857
[18] Cromer D T and Mann J B 1967 *J. Chem. Phys.* **47** 1892
[19] Sasaki S 1990 *KEK Report* 90-16
[20] *International Tables for X-ray Crystallography* 1962 vol 3, ed C H MacGillavry and G D Rieck (Birmingham: Kynoch) pp 175–92, pp 202–7
[21] Isshiki M *et al* 2001 *Proc. SRI2000* at press
[22] Soldo Y, Hazemann J L, Aberdam D, Inui M, Tamura K, Raoux D, Pernot E, Jal J F and Dupuy-Philon J 1998 *Phys. Rev.* B **57** 258
[23] Hosokawa S, Tamura K, Inui M, Yao M, Endo H and Hoshino H 1992 *J. Chem. Phys.* **97** 786
[24] Tamura K, Inui M and Hosokawa S 1995 *Rev. Sci. Instrum.* **66** 1382
[25] Gözlaff W, Schönherr G and Hensel F 1988 *Z. Phys. Chem., NF* **156** 219
Gözlaff W 1988 *PhD Thesis* University of Marburg
[26] Schmutzler R W and Hensel F 1972 *Ber. Bunsenges. Phys. Chem.* **76** 53
[27] Schönherr G, Schmutzler R W and Hensel F 1976 *Phil. Mag.* B **40** 411
[28] Yao M and Endo H 1982 *J. Phys. Soc. Japan* **51** 966
[29] Duckers L J and Ross R G 1972 *Phys. Lett.* A **38** 291
[30] Neale F E and Cusack N E 1979 *J. Phys. F: Met. Phys.* **9** 85
[31] Yao M and Endo H 1982 *J. Phys. Soc. Japan* **51** 1504
[32] Even U and Jortner J 1972 *Phil. Mag.* **25** 715
Even U and Jortner J 1973 *Phys. Rev.* B **8** 2536
[33] Ikezi H, Schwarzenegger K, Simons A L, Passner A L and McCall S L 1978 *Phys. Rev.* B **18** 2494
[34] Hefner W, Schmutzler R W and Hensel F 1980 *J. Physique Coll.* **41** C8 62
[35] Uchtmann H and Hensel F 1975 *Phys. Lett.* A **53** 239

Uchtmann H, Brusius U, Yao M and Hensel F 1988 *Z. Phys. Chem., NF* **156** 151

[36] Yao M, Takehana K and Endo H 1993 *J. Non-Cryst. Solids* **156–158** 807

[37] El-Hanany U and Warren W W Jr 1975 *Phys. Rev. Lett.* **34** 1276

[38] Devillers M A C and Ross R G 1975 *J. Phys. F: Met. Phys.* **5** 73

[39] Overhof H, Uchtmann H and Hensel F 1976 *J. Phys. F: Met. Phys.* **6** 523

[40] Fritzson P and Berggren K-F 1976 *Solid State Commun.* **19** 385

[41] Mattheis L F and Warren W W Jr 1977 *Phys. Rev.* B **16** 624

[42] Bosio L, Cortes R and Segaud C 1979 *J. Chem. Phys.* **71** 3595

[43] Pings C J 1968 *Physics of Simple Liquids* ed H N V Temperley, J S Rowlinson and G S Rushbrooke (Amsterdam: North-Holland) pp 405–11

[44] Winans J G and Heitz M P 1952 *Z. Phys.* **133** 291
Winans J G and Heitz M P 1953 *Z. Phys.* **135** 406

[45] Warren W W Jr and Hensel F 1982 *Phys. Rev.* B **26** 5980

[46] Nield V M and Verronen P T 1998 *J. Phys.: Condens. Matter* **10** 8147

[47] Arai T and McGreevy R L 1998 *J. Phys.: Condens. Matter* **10** 9221

[48] Franz J R 1986 *Phys. Rev. Lett.* **57** 889

[49] Kresse G and Hafner J 1997 *Phys. Rev.* B **55** 7539

[50] Hosokawa S, Kuboi T and Tamura K 1997 *Ber. Bunsenges. Phys. Chem.* **101** 120

[51] Hoshino H, Schmutzler R W and Hensel F 1976 *Ber. Bunsenges. Phys. Chem.* **80** 27

[52] Hoshino H, Schmutzler R W, Warren W W Jr and Hensel F 1976 *Phil. Mag.* **33** 255

[53] Endo H, Hoshino H, Schmutzler R W and Hensel F 1977 *Liquid Metals* ed R Evans and D A Greenwood (Bristol: Institute of Physics Publishing) p 412

[54] Warren W W Jr and Dupree R 1980 *Phys. Rev.* B **22** 2257

[55] Seyer H-P, Tamura K, Hoshino H, Endo H and Hensel F 1986 *Ber. Bunsenges. Phys. Chem.* **90** 587

[56] Ikemoto H, Yamamoto I, Yao M and Endo H 1994 *J. Phys. Soc. Japan* **63** 1611

[57] Hosokawa S and Tamura K 1990 *J. Non-Cryst. Solids* **117+118** 489

[58] Perron J C, Rabit J and Rialland J F 1982 *Phil. Mag.* B **46** 321

[59] Freyland W and Cutler M 1980 *J. Chem. Soc. Faraday Trans.* **76** 756

[60] Fischer R, Schmutzler R W and Hensel F 1980 *J. Non-Cryst. Solids* **35+36** 1295

[61] Hosokawa S and Tamura K 1990 *J. Non-Cryst. Solids* **117+118** 52

[62] Cabane B and Friedel J 1971 *J. Physique* **32** 73

[63] Edeling M and Freyland W 1981 *Ber. Bunsenges. Phys. Chem.* **85** 1049

[64] Fukutome H 1984 *Prog. Theor. Phys.* **71** 1

[65] Harrison W A 1980 *Electronic Structure and Properties of Solids* (San Francisco, CA: Freeman) p 93

[66] Ohtani H, Yamaguchi T and Yonezawa F 1998 *J. Phys. Soc. Japan* **67** 2807

[67] Shimojo F, Hoshino K, Watabe M and Zempo Y 1998 *J. Phys.: Condens. Matter* **10** 1199

[68] Kirchhoff F, Kresse G and Gillan M J 1998 *Phys. Rev.* B **57** 10 482

[69] Bichara C, Raty J-Y and Gaspard J-P 1999 *J. Non-Cryst. Solids* **250–252** 419

[70] Inui M, Tamura K, Oh'ishi Y, Nakaso I, Funakoshi F and Utsumi W 1999 *J. Non-Cryst. Solids* **250–252** 519

[71] Springborg M and Jones R O 1988 *J. Chem. Phys.* **88** 2652

[72] Inui M, Tamura K, Hazemann J L, Raoux D, Soldo Y, Argoud R and Jal J F 1999 *J. Non-Cryst. Solids* **250–252** 525

[73] Inui M, Oh'ishi Y, Nakaso I, Kazi M H and Tamura K 1999 *J. Non-Cryst. Solids* **250–252** 531

[74] Shimojo F, Hoshino K, Watabe M and Zempo Y 1999 *J. Phys.: Condens. Matter* **11** 8829